Received: 20 August 2023 | Revised: 27 September 2023 | Accepted: 9 October 2023

DOI: 10.1002/agt2.448

Aggregate Open Access WILEY

RESEARCH ARTICLE

Plasmon-enhanced FRET biosensor based on Tm^{3+}/Er^{3+} co-doped core-shell upconversion nanoparticles for ultrasensitive virus detection

Xinyue Lao[1] | **Yuan Liu**[1] | **Lihua Li**[1] | **Menglin Song**[1] | **Yingjin Ma**[1] | **Mo Yang**[2] | **Guanying Chen**[3] | **Jianhua Hao**[1]

[1]Department of Applied Physics, The Hong Kong Polytechnic University, Kowloon, Hong Kong, China

[2]Department of Biomedical Engineering, The Hong Kong Polytechnic University, Kowloon, Hong Kong, China

[3]MIIT Key Laboratory of Critical Materials Technology for New Energy Conversion and Storage, School of Chemistry and Chemical Engineering and Key Laboratory of Micro-systems and Micro-structures, Ministry of Education, Harbin Institute of Technology, Harbin, China

Correspondence
Jianhua Hao, Department of Applied Physics, The Hong Kong Polytechnic University, Kowloon 999077, Hong Kong, China.
Email: jh.hao@polyu.edu.hk

Funding information
Research Grants Council of the Hong Kong Special Administrative Region, China, Grant/Award Number: C5110-20GF; PolyU Internal Research Fund, Grant/Award Numbers: 1-CD4S, 1-W21G; Shenzhen-Hong Kong-Macau Technology Research Programme Fund, Grant/Award Number: SGDX2020110309260000

Abstract

Outbreaks of infectious viruses offer a formidable challenge to public healthcare systems and early detection of viruses is essential for preventing virus propagation. In this work, an ultrasensitive plasmon-enhanced fluorescence resonance energy transfer (FRET) biosensor based on core-shell upconversion nanoparticle (csUCNP) and gold nanoparticle (AuNP) for accurate detection of SARS-CoV-2 viral RNA is presented. In this biodetection assay, the Tm^{3+}/Er^{3+} co-doped csUCNP $NaGdF_4$:Yb/Tm@$NaYF_4$:Yb/Er acts as an energy donor and AuNP serves as an energy acceptor. The upconversion emission of Tm^{3+} and the design of the core-shell structure led to a simultaneous surface plasmon effect of AuNP. The localized surface plasmon resonance (LSPR) arising from collective oscillations of free electrons significantly enhanced FRET efficiency between Er^{3+} and AuNP. The as-prepared biosensor obtained a limit of detection (LOD) as low as 750 aM, indicating that the integration of FRET and surface plasmon into one biodetection assay significantly boosted the sensitivity of the biosensor. In addition, samples extracted from clinical samples are also utilized to validate the effectiveness of the biosensor. Therefore, this innovative plasmon-enhanced FRET biosensor based on Tm^{3+}/Er^{3+} co-doped csUCNP may pave the way for rapid and accurate biodetection applications.

KEYWORDS

biosensor, fluorescence resonance energy transfer, localized surface plasmon resonance, upconversion nanoparticles, virus detection

1 | INTRODUCTION

Infectious viruses are one of the greatest hazards to public health that human communities face. Since December 2019, the worldwide pandemic coronavirus disease 2019 (COVID-19) caused by the severe acute respiratory syndrome coronavirus 2 (SARS-CoV-2) has claimed the lives of more than 6 million people and caused 759 million total cases all over the world, posing a significant negative impact on the lives of individuals as well as the development of the global economy.[1,2] In addition, other viruses, such as Ebola virus, Human immunodeficiency virus, and Middle East respiratory syndrome coronavirus, also spread widely and cause debilitating illnesses.[3] However, current reliable and accessible techniques for virus detection and analysis, such as reverse transcription polymerase chain reaction (RT–PCR) and immunoassay methods (IA),[4] are time-consuming, high-cost, and highly dependent on laboratory equipment. As for the rapid antigen test (RAT), the alternative virus detection method has the drawbacks of low sensitivity and the potential for false negative results.[5] Detection and diagnosis of viruses at an early stage are essential for minimizing the threat caused by viruses. Therefore, it is crucial to construct a rapid and sensitive virus detection method to cut off the chain of viral transmission and minimize the infection.

Fluorescence resonance energy transfer (FRET) is a distance-dependent (2–10 nm) nonradiative energy transfer process between energy donor and energy acceptor pairs.[6–8] FRET has been commonly used for biosensing as the luminescent intensity of fluorophore varies with the approach or separation of the energy pairs.[9–11] Lanthanide-doped upconversion nanoparticles (UCNPs) are capable of

This is an open access article under the terms of the Creative Commons Attribution License, which permits use, distribution and reproduction in any medium, provided the original work is properly cited.

© 2023 The Authors. *Aggregate* published by South China University of Technology; AIE Institute and John Wiley & Sons Australia, Ltd.

converting low energy near-infrared (NIR) light to high energy ultraviolet (UV) or visible light and exhibit unique upconversion luminescence properties such as large anti-Stokes shift, narrow emission band, high photostability and long luminescence lifetime.[12,13] Additionally, UCNPs that are triggered by low energy NIR irradiation cause minimal damage to biomarkers and living organisms, making UCNPs an extremely attractive nanomaterial for bioanalytical and biomedical applications.[14–16] Accordingly, UCNPs have been extensively utilized as the energy donor in FRET biosensors for the detection of biological samples.[17–19] The Au-based nanomaterials, such as Au nanospheres and Au nanorods, exhibit size/shape-controlled optical, electrical and catalytic properties, high extinction coefficient, as well as aggregation-dependent colour change.[20] The highly controllable size range and optical characteristics of Au-based nanoparticles have contributed to their widespread applicability and endow them as excellent candidates of acceptors in FRET biosensors.[21,22]

Increasing the efficiency of FRET is a viable strategy for enhancing the sensitivity of FRET sensors. FRET efficiency is highly influenced by spectral overlap between donor emission and acceptor absorption, as well as the distance between donor and acceptor. Major efforts have been made to improve the limit of detection (LOD) of FRET biosensors by optimizing the UCNP architecture, using appropriate energy accepter, and improving the biosensor design.[18,23] Surface plasmon resonance (SPR) describes the collective oscillations of the conduction electrons in metallic structures at resonant conditions. Localized surface plasmon resonance (LSPR) is one type of SPR which is localized to a metallic nanostructure with dimensions less than the wavelength of incident light.[24,25] LSPR can concentrate the incident electromagnetic (EM) field around the metallic nanostructure and influence the optical process, resulting in plasmon enhanced fluorescence (PEF), surface enhanced Raman scattering (SERS), as well as plasmon enhanced FRET (PE-FRET). PE-FRET provides the potential to enhance the FRET efficiency and thereby improve the sensitivity of biosensing. Hou et al. reported a novel self-assembled plasmonic substrate that can enhance FRET efficiency, enabling ultrasensitive detection of DNA hybridization and imaging in live cells with improved temporal and spatial resolution.[26] However, there has been a relatively small amount of research conducted on PE-FRET biosensors based on UCNPs for the detection of viruses.

Here, a highly sensitive PE-FRET biosensor for the detection of SARS-CoV-2 viral Ribose Nucleic Acid (RNA) is constructed by using core-shell UCNP (csUCNP) $NaGdF_4$:Yb/Tm@$NaYF_4$:Yb/Er as energy donor and gold nanoparticle (AuNP) as energy acceptor. The design of core-shell structure of UCNP and employing AuNP as the energy acceptor possess multiple attributes that are essential for improving the sensitivity of the biosensor. Er^{3+} was designed in the shell of UCNP, ensuring the distance between the energy donor and energy acceptor was suitable for FRET process. While the inner core UCNP $NaGdF_4$:Yb/Tm coupled with AuNP was intended to enable plasmon modulated FRET and improve the energy transfer efficiency between energy pairs.[26,27] With the increase of target oligonucleotide concentration, the quenching efficiency of the biosensor based on Tm^{3+}/Er^{3+} co-doped csUCNP exceeded 90%, which was much higher than that of FRET biosensors without plasmon enhancement. Consequently, the LOD of the biosensor was improved to 750 aM. Moreover, clinical sample containing SARS-CoV-2 viral RNA was also tested to further verify the sensitivity of the biosensor.

2 | RESULTS AND DISCUSSION

2.1 | Detection scheme

The detection scheme of this work is depicted in Scheme 1. An FRET and LSPR dual-effected PE-FRET biosensing system was fabricated for the sensitive detection of SARS-CoV-2 RNA, with the csUCNP $NaGdF_4$:Yb/Tm@$NaYF_4$:Yb/Er and AuNP as the probes. The oligonucleotide modified csUCNP and AuNP could be conjugated by target oligo to form csUCNP–AuNP composite, resulting in a shorter distance between csUCNP and AuNP. The Er^{3+} in the shell of the UCNP acted as the energy donor and AuNP served as the energy acceptor, leading to the FRET process occurring between csUCNP and AuNP. Hence, the upconversion emission could be quenched with the increase of the target sequence concentration. Furthermore, the energy transfer efficiency could be further enhanced through the coupling between the inner core of csUCNP and the LSPR of AuNP. As a result, the increased FRET efficiency significantly improved the LOD of the biosensor, which is an essential performance metric for biosensors.

2.2 | Synthesis and characterization of the nanoparticles

The core-shell UCNP was synthesized using co-precipitation method and transmission electron microscope (TEM) was utilized to characterize the morphology of the as-synthesized UCNP. The core UCNPs $NaGdF_4$:Yb/Tm exhibit a uniform hexagonal structure (Figure 1A) with an average dimension of 15.7 nm (Figure S1a). The corresponding high-resolution transmission electron microscope (HRTEM) image in Figure 1B demonstrates that the UCNP is highly crystalline, with a lattice space of 0.29 nm, corresponding to the (101) lattice plane of $NaGdF_4$:Yb/Tm. The subsequently synthesized csUCNPs $NaGdF_4$:Yb/Tm@$NaYF_4$:Yb/Er also exhibit a hexagonal structure with an average size of 28.8 nm, as shown in Figure 1C. The thickness of the shell is calculated to be ≈6.5 nm based on the size distribution results (Figure S1). Under the trigger of near-infrared (NIR) 980 nm laser, the emission peaks of the synthesized Tm^{3+}/Er^{3+} co-doped csUCNP were located at 451 nm (Tm^{3+}, $^1D_2 \rightarrow {}^3F_4$), 542 nm ($Er^{3+}$,$^2H_{11/2} \rightarrow {}^4I_{15/2}$) and 654 nm ($Er^{3+}$, $^4F_{9/2} \rightarrow {}^4I_{15/2}$), respectively (Figure 1F, blue curve).

Citrate-stabilized AuNPs with precisely regulated size were prepared and served as the energy acceptor probe in the PE-FRET detection system. As depicted in Figure 1D, the TEM image indicated that the uniform sphere AuNPs with an average size of 5 nm was successfully synthesized. The HRTEM of AuNP in Figure 1E revealed a lattice space of 0.23 nm, corresponding to the (111) lattice plane of AuNP. The resultant AuNPs processed a broad absorption in the visible region, with the absorption peak centred at 518 nm (Figure 1F, red curve). The absorption of AuNPs

26924560, 2024, 2, Downloaded from https://onlinelibrary.wiley.com/doi/10.1002/agt2.448 by HONG KONG POLYTECHNIC UNIVERSITY HU NG HOM, Wiley Online Library on [23/09/2024]. See the Terms and Conditions (https://onlinelibrary.wiley.com/terms-and-conditions) on Wiley Online Library for rules of use; OA articles are governed by the applicable Creative Commons License

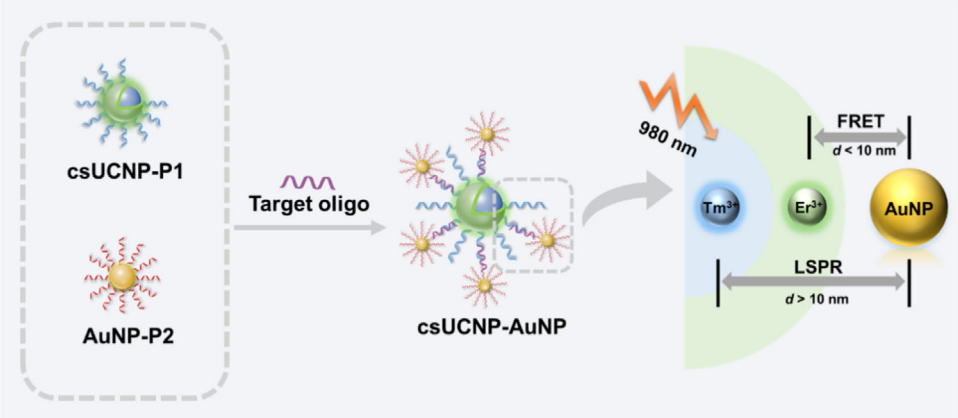

SCHEME 1 Schematic of the plasmon-enhanced FRET biodetection assay.

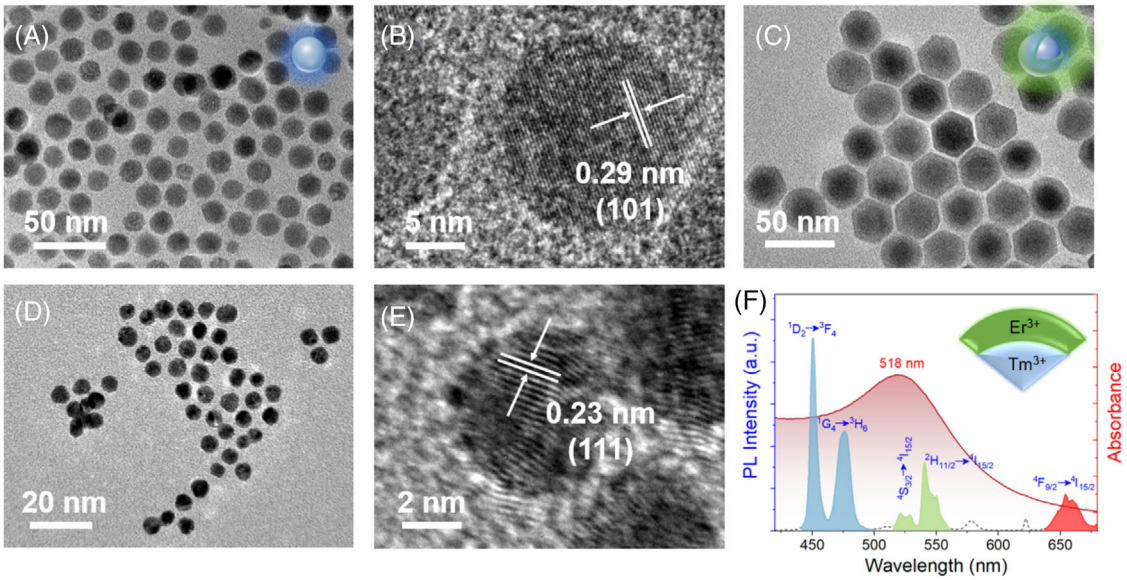

FIGURE 1 (A) TEM image of core UCNP $NaGdF_4$:Yb/Tm; (B) HRTEM image of core UCNP $NaGdF_4$:Yb/Tm; (C) TEM image of core-shell UCNP $NaGdF_4$:Yb/Tm@$NaYF_4$:Yb/Er; (D) TEM image of AuNP; (E) HRTEM image of AuNP; (F) upconversion emission spectrum of csUCNP (blue) and UV–vis absorption spectrum of AuNP (red).

matched well with the upconversion emission of Er^{3+}, assuring efficient energy transfer between csUCNP and AuNPs. Additionally, the upconversion emission of Tm^{3+} might operate as the incident light and trigger the LSPR of AuNPs. This would concentrate the electromagnetic (EM) field, which in turn increases the efficiency of FRET between the energy pairs.

2.3 | Sandwich biodetection assay

The N gene of SARS-CoV-2 was chosen as the target sequence for detection since the N gene sequence is conserved and less prone to mutation.[28] A 41-base oligonucleotide sequence was selected from the N gene sequence of SARS-CoV-2 based on a reported methodology.[29] Two oligonucleotides complementary to the target sequence are selected according to their banding energies, termed as P1 and P2, respectively. In order to modify the complementary oligonucleotides on the surface of csUCNP and AuNP, P1 is functionalized with amino groups at the 3′ end while P2 is with the sulphhydryl group, collectively called P1-NH_2 and P2-SH. P1-NH_2 will be further attached with csUCNP, and P2-SH will connect with AuNP to fabricate the sandwich biodetection assay. The target and complementary sequences with detailed base order information are displayed in Table S1.

Before constructing the sandwich biodetection assay, the oleate capped csUCNP (OA-csUCNP) will undergo several surface modification procedures, including acid treatment, surface carboxylation and conjugating with P1-NH_2, as illustrated in Figure 2A. The specific treatment procedures are described in supporting information. Zeta potential was utilized to verify the successful surface modification of csUCNP at each step, as displayed in Figure 2E. In addition, the UV–vis absorption spectrum of the oligonucleotide modified csUCNP exhibited an absorption peak at 260 nm (Figure 2B), which is the characteristic absorption peak of the oligonucleotide, also indicating that P1-NH_2 has been successfully attached on the surface of csUCNP. As for the construction of AuNP probe, the oligonucleotide P2-SH was connected on the surface of AuNP via forming solid gold–sulphur bonds.

26924560, 2024, 2, Downloaded from https://onlinelibrary.wiley.com/doi/10.1002/agt2.448 by HONG KONG POLYTECHNIC UNIVERSITY HU NG HOM, Wiley Online Library on [23/09/2024]. See the Terms and Conditions (https://onlinelibrary.wiley.com/terms-and-conditions) on Wiley Online Library for rules of use; OA articles are governed by the applicable Creative Commons License

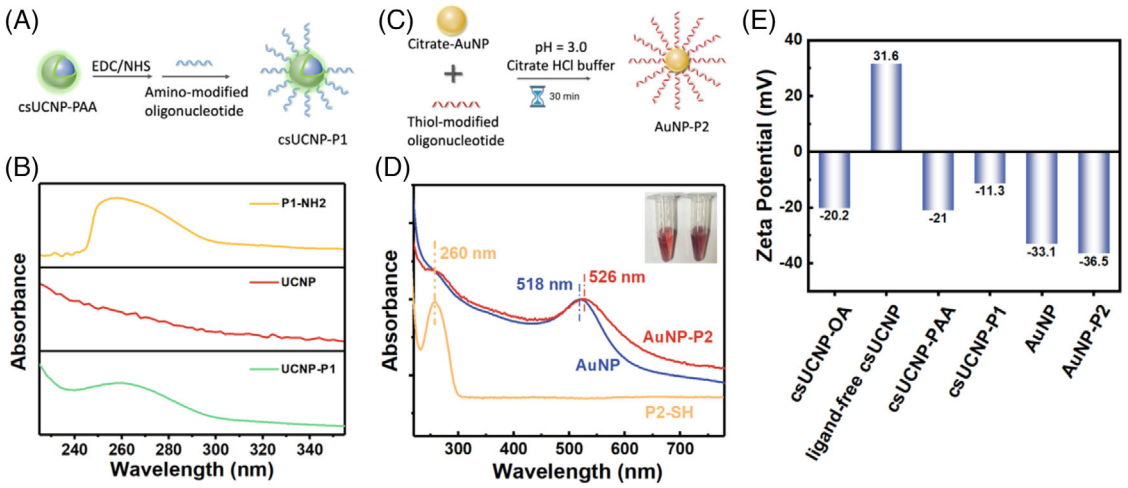

FIGURE 2 (A) Schematics of attaching amino-modified oligonucleotide to csUCNP-PAA; (B) UV–vis spectra of P1-NH_2, csUCNP, and csUCNP-P2; (C) schematics of attaching thiol-modified oligonucleotide to AuNP; (D) UV–vis spectra of P2-SH, AuNP and AuNP-P2 (inset are the photo of AuNP and AuNP-P2); (E) Zeta potential for the relative nanoparticles.

The simplified bonding procedure can be completed within 30 min using a pH-assisted method,[30] which involved the addition of a citrate–HCl buffer (pH = 3). The process diagram is depicted in Figure 2C. Figure 2D shows the normalized UV–vis absorption spectra of AuNP before and after the P2-SH modification (AuNP-P2). The presence of an oligonucleotide absorption peak at 260 nm in the absorption spectrum of AuNP-P2 indicates the successful attachment of oligo on the surface of AuNP. In addition, the absorption peak of AuNP at 518 nm is slightly red shifted to 526 nm after the connection. Correspondingly, the aggregation of AuNPs also causes a change in the colour of the solution from pink to light purple (inset of Figure 2D, left: AuNPs, right: AuNP-P2). The mismatch of the absorption spectra and the observed alteration in the colour of the solution can be attributed to the slight aggregation of AuNPs. Since the intense aggregation of AuNPs will affect the detection result, the aggregation of AuNPs has been minimized by adjusting the AuNP-to-oligonucleotide ratio and the concentration of citrate buffer. Moreover, the zeta potential of AuNP changed from −33.1 to −36.5 mV after connected with the oligonucleotide P2-SH, which can be attributed to the replacement of citrate ligands on the surface of AuNP by P2-SH, as displayed in Figure 2E. The surface potentials of csUCNP-P1 and AuNP-P2 are both negative, thus there was no electronic attraction among the probes.

2.4 | SARS-CoV-2 RNA detection

Figure 3A shows the schematic of the biodetection procedure in this work. The csUCNP-P1 and AuNP-P2 probes were first added in a centrifuge tube and AuNP-P2 could partially suppress the upconversion emission of the UCNPs. With an increase in the amount of AuNPs, the emission of csUCNPs could be reduced to a greater extent. The quenching effect may be caused by the broad peak absorption of AuNPs, which can absorb a portion of the 980 nm excitation light, thus leading to the reduction of upconversion emission intensity. Therefore, the amount of csUCNPs and AuNPs were fixed while detecting the variation of N target sequence concentration. It is worth noting that during the detection procedure, it is possible to disregard the variation in upconversion emission intensity caused by the varying target concentration or solution volume (Figure S2). As P1 and P2 are complementary to the target N sequence, csUNCP-P1 and AuNP-P2 can be conjugated by the N target sequence. After the conjugation, the distance between csUNCPs and AuNPs became shorter (as shown in the inset of Figure 3B), thus leading to an efficient FRET process and resulting in a significant quenching effect of upconversion emission. The insets of Figure 3A depicted the corresponding confocal microscopy images of csUCNP before and after the hybridization upon the 980 nm excitation (scale bar = 50 μm). The upconversion emission of Er^{3+} (green) and Tm^{3+} (blue) are apparently weaker after the hybridization with the *N* target sequences.

The amount of AuNP attached to the surface of csUCNP increased with the increasing concentration of *N* target sequence in the biodetection system, leading to an enhanced quenching effect with reference to the concentrations of target sequence. As shown in Figure 3B, the upconversion emission of csUCNP decreased significantly as the concentration of the N target sequence increased from 0 to 1 nM during the detection process. The inset of Figure 3B depicts the TEM image of the detection sample, in which csUCNP is surrounded by several AuNPs, indicating the conjugation between AuNPs and csUCNP. Figure 3C–E shows the quenching efficiency of the upconversion emission peaks at 451, 542, and 654 nm, respectively. Apparently, the quenching efficiency significantly increased with the increase of the N target sequence. In addition, the quenching efficiency of csUCNP exceeds 90% with 1 nM target oligo, which is much higher than that of the FRET biosensor based solely on Er^{3+} doped UCNP, as shown in Table 1.

To evaluate the optimal incubation condition, the biosensor based on Tm^{3+}/Er^{3+} co-doped csUCNP was evaluated at the N target sequence concentration of 1 pM with varying incubation temperatures. The incubation time was varied from 10 to 40 min with a 10-min interval, and three incubation temperature at room temperature (20°C), 40 and 55°C was selected for comparison. As shown in Figure S3–S5, the quenching efficiency of csUCNP reached a maximum of nearly 90% after 40 min incubation at 55°C. For comparison, $NaYF_4$:Yb/Er probe and $NaGdF_4$:Yb/Tm probe were

26924560, 2024, 2, Downloaded from https://onlinelibrary.wiley.com/doi/10.1002/agt2.448 by HONG KONG POLYTECHNIC UNIVERSITY HU NG HOM, Wiley Online Library on [23/09/2024]. See the Terms and Conditions (https://onlinelibrary.wiley.com/terms-and-conditions) on Wiley Online Library for rules of use; OA articles are governed by the applicable Creative Commons License

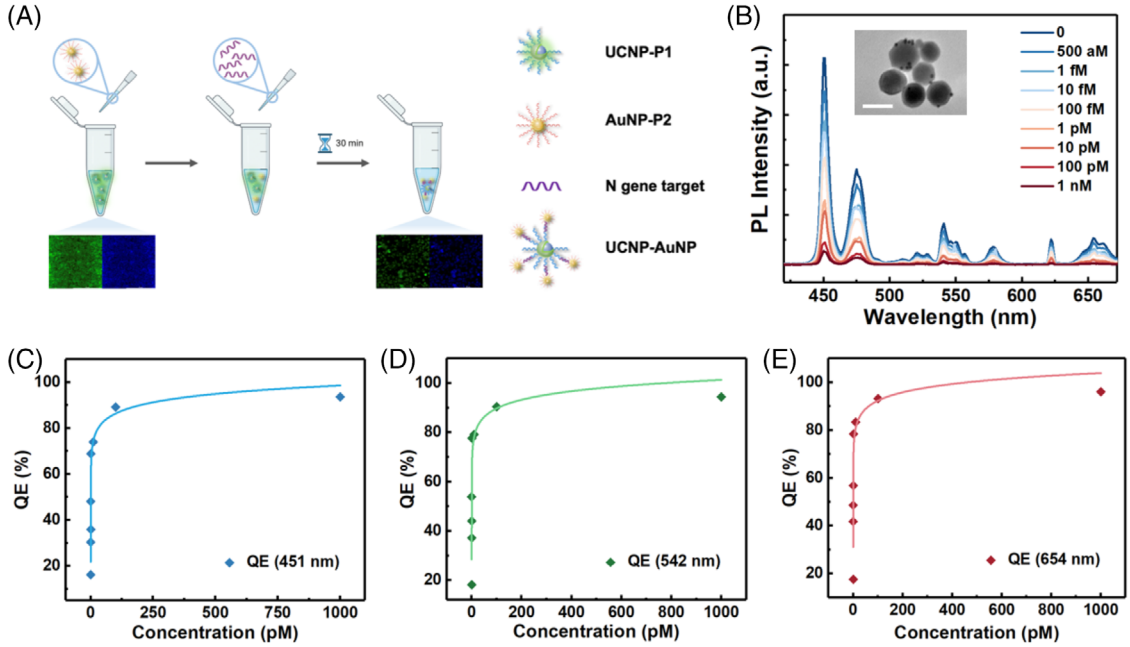

FIGURE 3 (A) Schematic of the biodetection procedure; (B) upconversion spectra of csUCNP probe with various concentrations of SARS-CoV-2 target sequence in the sandwich detection assay, the inset was the TEM image of the detection sample (scale bar = 50 nm); quenching efficiency of three major upconversion emission peaks at (C) 451 nm, (D) 542 nm and (E) 654 nm with various concentration of SARS-CoV-2 target sequence.

TABLE 1 Comparison of common FRET biosensors based on UCNPs.

Type of UCNPs	Accepter	Surface functionalized	Target	LOD	Detection range	Ref.
$NaYF_4$:Yb,Er	Quantum dots	Streptavidin	biotin	5 nM	1–1 μM	[31]
$NaYF_4$:Yb,Tm	SYBR Green I	ssDNA1	ssDNA2	3.2 nM	10–200 nM	[32]
$NaYF_4$:Yb,Er	AuNPs	Oligonucleotides	long-chain DNA sequence	3 nM	0–60 nM	[33]
$NaYF_4$:Yb,Er@$NaYF_4$	Cy3 dye	ssDNA	miR20a	30 pM	0.1–100 nM	[34]
$NaYF_4$:Yb,Er	Gold nanorods	ssDNA	DNA	7 pM	0–100 nM	[35]
$BaGdF_5$:Yb/Er	AuNPs	Oligonucleotides	Ebola Virus RNA	300 fM	3–50 pM	[36]
$NaGdF_4$:Yb/Er@ $NaGdF_4$	AuNPs	Oligonucleotides	SARS-CoV-2 RNA	11.46 fM	200 fM–10 nM	[37]
$NaGdF_4$:Yb/Tm@ $NaYF_4$:Yb/Tm	AuNPs	Oligonucleotides	SARS-CoV-2 RNA	750 aM	1 fM–1 nM	This work

also constructed and applied for detection under the same incubation condition. In contrast, the quenching efficiency of $NaYF_4$:Yb/Er UCNP reached only 48% at the incubation temperature of 55°C (Figure S6), whereas the upconversion emission intensity of $NaGdF_4$:Yb/Tm probe exhibits only a slight decrease (Figure S7). The enhanced quenching efficiency against the target sequence concentration leads to an enhanced sensitivity for biosensor. Consequently, such a comparative study indicated that the design of core-shell structure and the co-doping of Tm^{3+} and Er^{3+} can significantly improve the sensitivity of biosensor based on UCNP probes, hence a lower LOD can be further obtained.

A possible causation of such high quenching efficiency is that the localized surface plasmons enhanced the energy transfer efficiency between energy pairs. The schematic of the mechanic in the PE-FRET biosensor based on oligo conjugated csUCNP-AuNP is displayed in Figure 4A, and the energy migration processes of $Yb^{3+} \rightarrow Er^{3+}$ and $Yb^{3+} \rightarrow Tm^{3+}$ in the csUCNP under the excitation of 980 nm are exhibited in Figure 4B. Specifically, Yb^{3+} is an ideal sensitizer for 980 nm excitation owing to the $^2F_{7/2} \rightarrow {}^2F_{5/2}$ transition, which well matches the electronic transitions of Er^{3+} and Tm^{3+}. The upconversion emission of Er^{3+} in the shell observed at 542 and 654 nm are ascribed to the $^2H_{11/2} \rightarrow {}^4I_{15/2}$ and $^4F_{9/2} \rightarrow {}^4I_{15/2}$ transitions. While the inner core upconversion emission of Tm^{3+} at 451 nm is attributed to $^1D_2 \rightarrow {}^3F_4$ transition. Furthermore, the core-shell structure enabled different doping concentrations for Yb^{3+}/Tm^{3+} and Yb^{3+}/Er^{3+}, respectively. Plenty of research have proved that metal nanostructures could induce plasmon-enhanced upconversion emission, as the local electric field around metal nanostructures can promote the excitation rate of lanthanide sensitizer ions, leading to enhanced

26924560, 2024, 2, Downloaded from https://onlinelibrary.wiley.com/doi/10.1002/agt2.448 by HONG KONG POLYTECHNIC UNIVERSITY HU NG HOM, Wiley Online Library on [23/09/2024]. See the Terms and Conditions (https://onlinelibrary.wiley.com/terms-and-conditions) on Wiley Online Library for rules of use; OA articles are governed by the applicable Creative Commons License

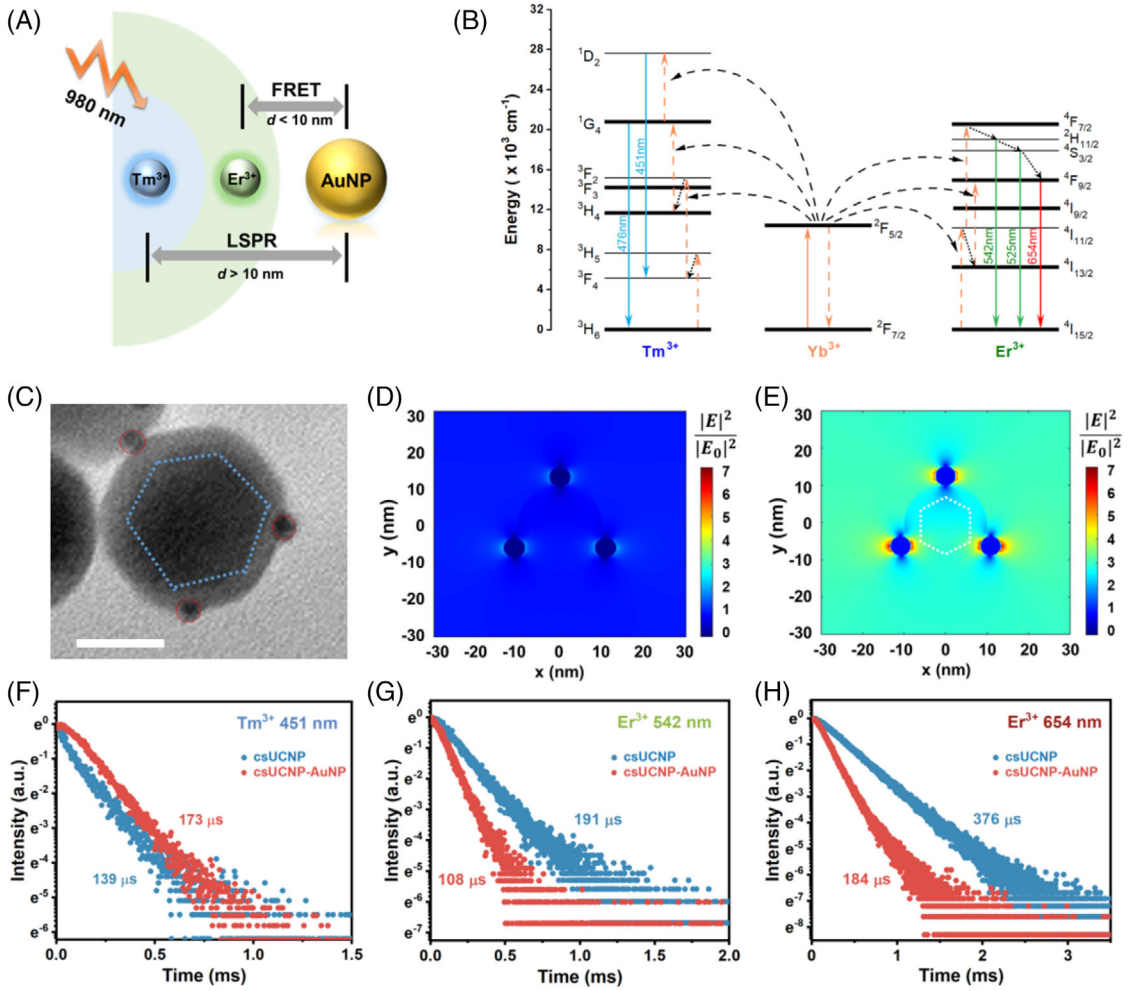

FIGURE 4 (A) Schematic of the mechanics in the PE-FRET biosensor based on csUCNP and AuNP; (B) corresponding energy transfer routes of the csUCNP; (C) TEM image of oligo conjugated csUCNP-AuNP (scale bar = 20 nm); Simulated local electromagnetic field distribution of AuNPs by FDTD method (D) without the core emission; (E) with the core emission of Tm^{3+} at 451 nm. Luminescence decay curves of csUCNP and conjugated csUCNP-AuNP at (F) 451 nm; (G) 542 nm; (H) 654 nm.

upconversion emission.[38–41] While there are additional studies demonstrating that surface plasmon could enhance FRET efficiency as well.[42,43] Specifically, the energy transfer efficiency could be calculated by the following equation[44]:

$$E = 1 - \frac{F}{F_0} = \frac{R_0^6}{R_0^6 + r^6} \quad (1)$$

where F and F_0 are the upconversion emission intensities of UCNP before and after quenched by AuNP, r is the distance between the energy donor and the energy accepter, and R_0 is the Förster distance at which the 50% of energy is transferred. R_0 depends on a variety of factors, including the overlap of donor emission and acceptor absorption, donor quantum yield, and the orientation of transition dipole moments. Since LSPR will contribute to an increase in the Förster distance, the energy transfer efficiency would consequently increase.[43,45] Therefore, the LSPR of AuNPs induced by Tm^{3+} upconversion emission improved the performance of the biosensor by enhancing the FRET efficiency, resulting in a higher detection sensitivity.

The electromagnetic field distribution of AuNPs under different situations were simulated by the Finite-Difference Time-Domain (FDTD) method and compared for illustration. The simulation model was established according to TEM image of oligo conjugated csUCNP-AuNP composite in Figure 4C. E/E_0 is utilized for demonstrating the variation of electromagnetic field intensity around gold nanoparticles with and without the core upconversion emission, where E is the value of local electromagnetic field and E_0 is the value of incident electric field. Figure 4D,E present the electromagnetic field intensities of AuNP around UCNP without and with the core upconversion emission of Tm^{3+}, respectively. The electromagnetic field intensities around AuNPs are obviously increased when Tm^{3+} upconversion emission in the core of csUCNP is present. According to the previous research, the local electromagnetic field can influence the orientation of these dipoles, and thus influence the FRET efficiency.[46] Hence, the sensitivity of the presented PE-FRET biosensor was significantly enhanced by the design of core-shell structure and doping with Tm^{3+} in the inner core.

The decay times of the three main upconversion emission peaks (451, 542, 654 nm) were measured to further illustrate the energy transfer process between csUCNP and AuNP, as displayed in Figure 4F–H. The decay curves could be well fitted by the following biexponential function

26924560, 2024, 2, Downloaded from https://onlinelibrary.wiley.com/doi/10.1002/agt2.448 by HONG KONG POLYTECHNIC UNIVERSITY HU NG HOM, Wiley Online Library on [23/09/2024]. See the Terms and Conditions (https://onlinelibrary.wiley.com/terms-and-conditions) on Wiley Online Library for rules of use; OA articles are governed by the applicable Creative Commons License

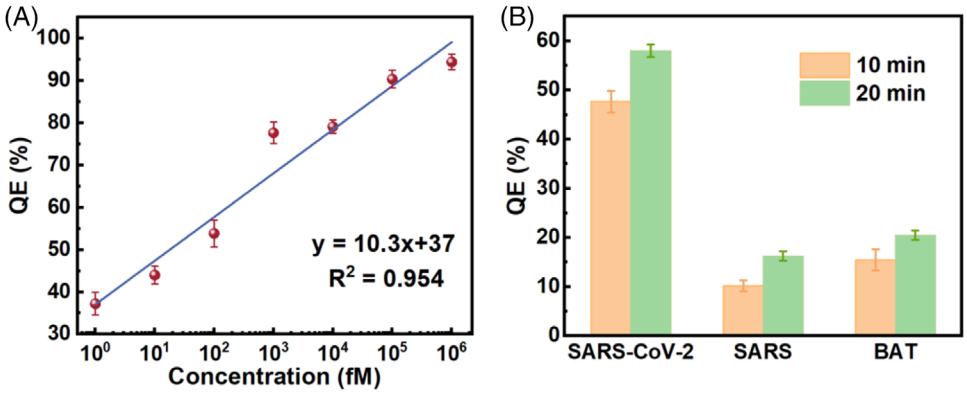

FIGURE 5 (A) Linear relationship of the sandwich assay based on csUCNP against different concentration of target sequence from 1 fM to 1 nM; (B) specificity of the sandwich assay with the non-target oligonucleotide sequence concentration of 1 pM.

(Equation (2)) and the fitted decay curves are displayed in Figure S8.

$$I(t) = A_1 \exp\left(-\frac{t}{\tau_1}\right) + A_2 \exp\left(-\frac{t}{\tau_2}\right) \quad (2)$$

$$\tau^* = \frac{A_1\tau_1^2 + A_2\tau_2^2}{A_1\tau_1 + A_2\tau_2} \quad (3)$$

where $I(t)$ is the photoluminescence intensity, A_1 and A_2 are corresponding fitting constants, τ_1 and τ_2 are rapid and slow lifetimes of different exponential components. Then the average lifetime τ^* could be calculated by Equation (3).[47] The average lifetimes of the upconversion emission peak of Er^{3+} at 542 and 654 nm decreased from 191 to 108 μs and from 376 to 184 μs, respectively. The significant decrease in lifetime of Er^{3+} indicates the high efficiency FRET process between the upconversion emission of Er^{3+} and AuNPs. However, the average lifetime of upconversion emission peak of Tm^{3+} at 451 nm exhibits negligible changes, indicating that FRET between the inner core of csUCNP and AuNP is either non-existent or feeble. The slight decrease of lifetime of Tm^{3+} at 451 nm from 139 to 173 μs probably caused by coupling with LSPR of AuNP.

2.5 | Figure of merit

The linear response, LOD, and specificity are three typical characteristics of biosensors. Therefore, to illustrate the excellent performance of co-doped csUCNP biosensor, the three typical characteristics of the biosensor based on Tm^{3+}/Er^{3+} co-doped csUCNP were discussed in this section.

As shown in Figure 3B, the quenching efficiency of upconversion emission of csUCNP increased with the increase of N target sequence concentration. Therefore, a linear response could be found between the quenching efficiency and the concentration of target sequence. The linear fitting curve was displayed in Figure 5A, with the linear equation of $y = 10.3x + 37$, indicating that the csUCNP was suitable to serve as the probe for constructing the FRET biosensor. The LOD of the biosensor could be estimated by the following equation:

$$LOD = \frac{3\delta}{b} \quad (4)$$

where δ is the standard deviation and b is the slope of the linear fitting curve. Thereby, the LOD of csUCNP biosensor was calculated to be 750 aM, which was equivalent to 4.65×10^7 N target copies in 500 μL detection system volume. Compared to the reported biosensors based on Er-UCNPs, the doping of Tm^{3+} ions and the design of core-shell probes result in lower LODs of biological probes based on UCNPs.

The ability of the biosensor to recognize a particular target sequence is defined as specificity, and it is an essential component to consider when assessing the performance of the biodetection system. To examine the specificity of the biosensor based on csUCNP, a concentration of 1 pM of the N target sequence was selected for evaluation within the detection linear range. Two non-target gene sequences from the SARS and BAT viruses were subjected to comparative testing at the same concentration. According to the results of the specificity test in Figure 5B, the non-target gene sequence has a significantly lower quenching efficiency than the SARS-CoV-2 virus oligo. This indicates that the constructed bioprobes based on csUCNP has high level of specificity for SARS-CoV-2 virus.

Based on the above demonstration, csUCNP-based biosensors in this work exhibit low LOD as well as high sensitivity and specificity for the detection of SARS-CoV-2. The design of core-shell structure of UCNP significantly enhanced the performance for the application of biodetection.

2.6 | Detection of PCR-validated deactivated clinical sample

To further verify the feasibility of the csUCNP-based biosensor in clinical application, the performance of the biosensor on clinical sample detection was further tested. The RNA from inactivated SARS-CoV-2 virus sample used for clinical detection was obtained from the University of Hong Kong, Faculty of Medicine. Prior to the detection by csUCNP-based biosensor, RT-PCR was utilized to determine the concentration of the inactivated SARS-CoV-2 virus sample. A series of standard samples with different concentrations were running in the same RT-PCR procedure to generate the standard curve. The Ct value of the clinical sample was 23 (Figure 6A) and the concentration was determined to be 180 fM according to the standard curve. The clinical sample was diluted tenfold for detection by csUCNP-based biosensor. Figure 6B

26924560, 2024, 2, Downloaded from https://onlinelibrary.wiley.com/doi/10.1002/agt2.448 by HONG KONG POLYTECHNIC UNIVERSITY HU NG HOM, Wiley Online Library on [23/09/2024]. See the Terms and Conditions (https://onlinelibrary.wiley.com/terms-and-conditions) on Wiley Online Library for rules of use; OA articles are governed by the applicable Creative Commons License

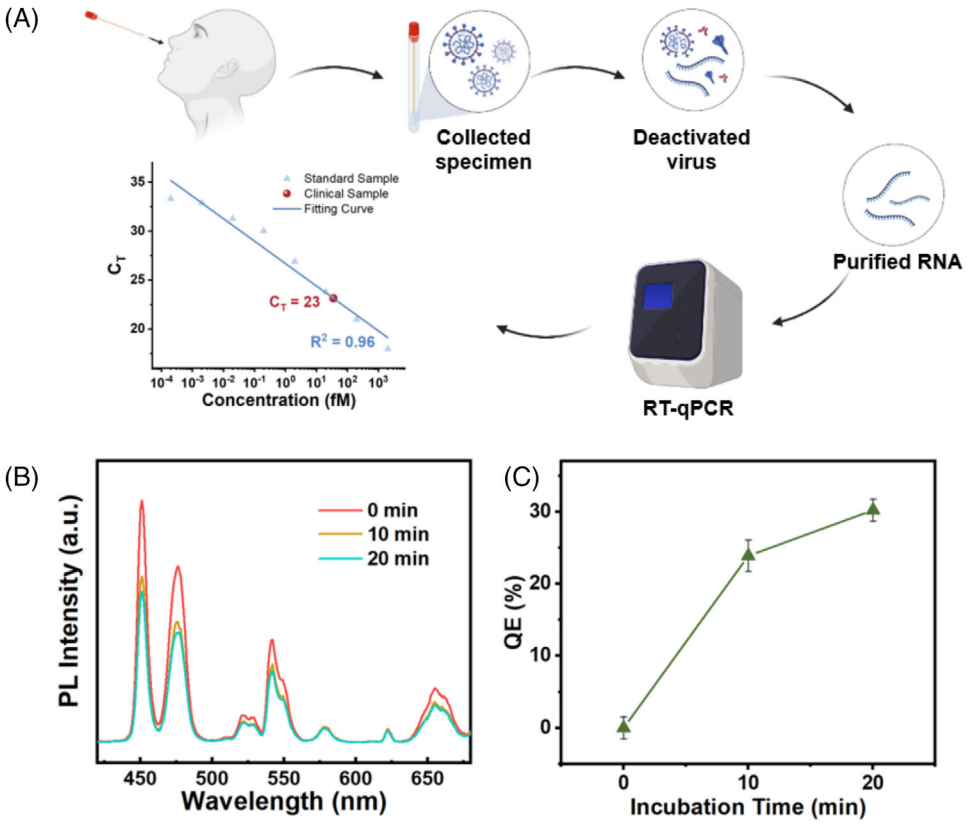

FIGURE 6 (A) Diagnostic testing through RT-PCR and the test results; (B) upconversion emission spectra and (C) quenching efficiency of the detection of deactivated clinical SRAS-CoV-2 sample based on csUCNP FRET biodetection assay.

is the time varying luminescence spectrum of the csUCNP at the SARS-CoV-2 RNA concentration of 18 fM. After incubation for 10 min, the fluorescence intensity decreased significantly and the relative quenching efficiency of the four upconversion emission peaks with respect to time was displayed in Figure 6B. The quenching efficiency of the upconversion emission peaks reached up to 30% at such a low target sequence concentration. The results demonstrate that the csUCNP-based biosensor constructed for the detection of SARS-CoV-2 clinical samples performs admirably.

3 | CONCLUSION

In summary, a plasmon-enhanced FRET biosensor based on UCNP with core-shell structure was proposed for ultrasensitive detection of SARS-CoV-2 viral RNA. After conjugation with the target sequence, the distance between csUCNPs and AuNPs was reduced, which activated the FRET process and effectively quenched upconversion emission. Simultaneously, the upconversion emission of Tm^{3+} in the inner core of csUCNP induced LSPR of AuNPs, leading to a significant increase of FRET efficiency. Consequently, the dual effect of LSPR and FRET results in higher sensitivity of biosensor based on csUCNP. The LOD of the PE-FRET biosensor was improved to 750 aM with decent linear response and good selectivity, which is much lower than that of biosensors based on Er-doped UCNP. In addition, the detection of RNA extracted from deactivated clinical sample using this biosensor was also performed with the LOD approaching femtomolar level, indicating the potential clinical application of the as-prepared biosensor. Overall, the results in this work illustrate that this plasmon-enhanced FRET biosensor based on csUCNP could be potential sensing platforms for instant and sensitive virus RNA detection.

4 | EXPERIMENTAL SECTION

4.1 | Materials

Lanthanide acetates including $Y(Ac)_3{\cdot}4H_2O$, $Gd(Ac)_3{\cdot}4H_2O$, $Yb(Ac)_3{\cdot}4H_2O$, $Tm(Ac)_3{\cdot}4H_2O$, $Er(Ac)_3{\cdot}4H_2O$, NH_4F, 1-octacene (ODE), oleic acid (OA), cyclohexane, hydrochloric acid (HCl, 37%) and Poly(acrylic acid) (PAA, M_w = 1800) were purchased from Sigma Aldrich. 1-Ethyl-3-(3-dimethylaminopropyl)-carbodiimide hydrochloride (EDC), *N*-hydroxysulphosuccinimide sodium salt (sulpho-NHS) and tetrachloroauric acid ($HAuCl_4$) were obtained from TCI. Sodium citrate, potassium carbonate (K_2CO3), tannic acid, NaOH, dithiothreitol (DTT), 2-(*N*-morpholino)ethanesulphonic acid (MES) were purchased from Aladdin. DNA oligos were purchased from the University of Hong Kong, Faculty of Medicine, LKS Center for PanorOmic Sciences. All the above chemicals were used without further purification. DEPC water was used for all the procedures involving oligonucleotides (oligos).

4.2 | Synthesis of the core $NaGdF_4$:Yb/Tm nanocrystals

The core UCNP $NaGdF_4$:Yb/Tm were synthesized by the coprecipitation method according to a previously reported

26924560, 2024, 2, Downloaded from https://onlinelibrary.wiley.com/doi/10.1002/agt2.448 by HONG KONG POLYTECHNIC UNIVERSITY HU NG HOM, Wiley Online Library on [23/09/2024]. See the Terms and Conditions (https://onlinelibrary.wiley.com/terms-and-conditions) on Wiley Online Library for rules of use; OA articles are governed by the applicable Creative Commons License

article.[48] Lanthanide^{3+} (Ln^{3+}) acetates, including yttrium (Y), gadolinium (Gd), ytterbium (Yb), terbium (Tm), and erbium (Er) were dissolved in de-ionized (DI) water to form 0.2 M aqueous solution for further usage. In a typical synthesis procedure, 1 mL of 0.2 M $Gd(CH_3COO)_3$, 0.98 mL of 0.2 M $Yb(CH_3COO)_3$, 0.02 mL of 0.2 M $Tm(CH_3COO)_3$, 4 mL of OA and 6 mL of ODE were added into a 50-mL flask. Under magnetic stirring (1500 rpm), the solution was slowly heated from room temperature to 150°C and maintained for 40 min. Then the reaction mixture was allowed to cool to room temperature after removing the heating mantle. At room temperature, a mixture of 1 mL of 1 M NaOH-methanol solution and 3.3 mL of 0.4 M NH_4F-methanol solution was quickly injected into the reaction flask after 10 s of vortex. The mixture was then heated to 50°C and maintained for 30 min with vigorous stirring to evaporate methanol. After that, the mixture was heated to 100°C, followed by a 10-min vacuum degassing to evaporate the residual moisture and methanol. The flask was then heated to 290°C at a rate of 10°C/min under the protection of argon gas and maintained for 1.5 h before cooling to room temperature. The synthesized UCNPs were precipitate by adding 5 mL of ethanol and collected by centrifugation. The UCNPs were further purified with cyclohexane and ethanol three times and dispersed in cyclohexane for the synthesis of core-shell UCNPs.

4.3 | Synthesis of the core–shell $NaGdF_4$:Yb/Tm@$NaYF_4$:Yb/Er UCNPs

The core-shell $NaGdF_4$:Yb/Tm@$NaYF_4$:Yb/Er UCNPs were synthesized approximately the same as the procedure of core UCNPs. Briefly, 1.6 mL of 0.2 M $Y(CH_3COO)_3$, 0.36 mL of 0.2 M $Yb(CH_3COO)_3$, 0.04 mL of 0.2 M $Er(CH_3COO)_3$, 4 mL of OA and 6 mL of ODE were added into a 50-mL flask. Under magnetic stirring (1500 rpm), the solution was slowly heated from room temperature to 150°C and maintained for 40 min. Then the reaction mixture was allowed to cool to room temperature after removing the heating mantle. At room temperature, the as-prepared core UCNPs $NaGdF_4$:Yb/Tm were injected into the flask. Then, a mixture of 1 mL of 1 M NaOH-methanol solution and 3.3 mL of 0.4 M NH_4F-methanol solution was quickly injected into the reaction flask after 10 s of vortex. The mixture was heated to 50°C and maintained for 30 min with vigorous stirring and then heated to 100°C followed by a 10-min vacuum degassing. The flask was then heated to 290°C at a rate of 10°C/min under the protection of argon gas and maintained for 1.5 h before cooling down to room temperature. The synthesized csUCNPs were precipitate by adding 5 mL of ethanol and collected by centrifugation. The csUCNPs were further purified with cyclohexane and ethanol three times for surface modification.

4.4 | Synthesis of citrate-stabilized AuNPs

The citrate-stabilized AuNPs were synthesized according to the previous report.[49] Briefly, tannic acid (20 μL, 2.5 mM), potassium carbonate (200 μL, 150 mM) and sodium citrate solution (30 mL, 2.2 mM) were added to a 50 mL flask under vigorous stirring. The mixture was heated to 70°C and 100 μL $HAuCl_4$ (25 mM) was added two times every 10 min interval. The solution then turns pink and naturally cools to room temperature for continued use.

4.5 | Surface modification of csUCNP

The as-synthesized csUCNP was precipitated in 15 mL ethanol with addition of 112 μL HCl (2 M). After sonication for 30 min, the csUCNPs were precipitated by centrifugation and redispersed in 15 mL ethanol. After that, 11.2 μL HCl (2 M) was added and sonicated for 30 min. Then the ligand-free csUCNP were collected by high-speed centrifugation. After that, PAA (20 mg) dissolved in NaOH (0.2 M) was added to the ligand-free csUCNPs. The colloidal solution was stirred overnight and PAA-csUCNPs were collected by high-speed centrifugation, followed by three successive purifications with water. The PAA-csUCNPs were dispersed in water (1 mL) for storage.

4.6 | Conjugation of csUCNP with amino modified oligos

PAA-csUCNPs (200 μL) was buffer-exchanged in MES buffer (pH 5, 500 μL). After that, EDC (3 mg) and NHS (6 mg) were added to the csUCNPs under stirring for 30 min. Then, 1 nmol of P2 was added to the tube and stirred for another 2.5 h to ensure complete coupling reaction. The csUCNPs-P2 was collected by high-speed centrifugation and washed with water for three times. The csUCNPs-P2 was then dispersed in water for further use.

4.7 | Conjugation of AuNPs with sulphhydryl oligos

DTT solution (10 μL, 0.1 M) was added to P1 (10 nmol) for S—S bond cleavage reaction for 1 h. The cleaved P1 was purified and recovered by illustra microspin G-25 column (GE Healthcare). Then, the AuNPs were modified with a previously reported instantaneous oligo modification.[30] The DTT-treated P1 (10 μL) was added to citrate-stabilized AuNPs (200 μL) with PB buffer (4 μL, 50 mM) and citrate buffer (pH 3, 10 μL). The mixture was incubated for 5 min and the AuNPs-P1 was recovered by high-speed centrifugation. The washing step was repeated for three times. The AuNPs-P1 was dispersed in water (200 μL) for further use.

ACKNOWLEDGEMENTS

This work was supported by the grant from the Research Grants Council of the Hong Kong Special Administrative Region, China (Project No. CRF No. PolyU C5110-20GF), PolyU Internal Research Fund (1-CD4S, 1-W21G) and the Shenzhen-Hong Kong-Macau Technology Research Programme Fund (SGDX2020110309260000).

CONFLICT OF INTEREST STATEMENT

The authors declare no conflicts of interest.

ORCID

Mo Yang https://orcid.org/0000-0002-3863-8187
Jianhua Hao https://orcid.org/0000-0002-6186-5169

26924560, 2024, 2, Downloaded from https://onlinelibrary.wiley.com/doi/10.1002/agt2.448 by HONG KONG POLYTECHNIC UNIVERSITY HU NG HOM, Wiley Online Library on [23/09/2024]. See the Terms and Conditions (https://onlinelibrary.wiley.com/terms-and-conditions) on Wiley Online Library for rules of use; OA articles are governed by the applicable Creative Commons License

REFERENCES

1. P. Zhou, X.-L. Yang, X.-G. Wang, B. Hu, L. Zhang, W. Zhang, H.-R. Si, Y. Zhu, B. Li, C.-L. Huang, H.-D. Chen, J. Chen, Y. Luo, H. Guo, R.-D. Jiang, M.-Q. Liu, Y. Chen, X.-R. Shen, X. Wang, X.-S. Zheng, K. Zhao, Q.-J. Chen, F. Deng, L.-L. Liu, B. Yan, F.-X. Zhan, Y.-Y. Wang, G.-F. Xiao, Z.-L. Shi, *Nature* **2020**, *579*, 270.
2. WHO Coronavirus (COVID-19) Dashboard. https://covid19.who.int/ (accessed: March **2023**).
3. R. E. Baker, A. S. Mahmud, I. F. Miller, M. Rajeev, F. Rasambainarivo, B. L. Rice, S. Takahashi, A. J. Tatem, C. E. Wagner, L.-F. Wang, A. Wesolowski, C. J. E. Metcalf, *Nat. Rev. Microbiol.* **2022**, *20*, 193.
4. N. Ravi, D. L. Cortade, E. Ng, S. X. Wang, *Biosens. Bioelectron.* **2020**, *165*, 112454.
5. A. Osterman, I. Badell, E. Basara, M. Stern, F. Kriesel, M. Eletreby, G. N. Öztan, M. Huber, H. Autenrieth, R. Knabe, P. M. Späth, M. Muenchhoff, A. Graf, S. Krebs, H. Blum, J. Durner, L. Czibere, C. Dächert, L. Kaderali, H.-M. Baldauf, O. T. Keppler, *Med. Microbiol. Immunol.* **2022**, *211*, 105.
6. L. Yuan, W. Lin, K. Zheng, S. Zhu, *Acc. Chem. Res.* **2013**, *46*, 1462.
7. J. Yao, M. Yang, Y. Duan, *Chem. Rev.* **2014**, *114*, 6130.
8. E. Lerner, T. Cordes, A. Ingargiola, Y. Alhadid, S. Chung, X. Michalet, S. Weiss, *Science* **2018**, *359*, eaan1133.
9. N. Melnychuk, S. Egloff, A. Runser, A. Reisch, A. S. Klymchenko, *Angew. Chem. Int. Ed.* **2020**, *59*, 6811.
10. A. Kaur, S. Dhakal, *TrAC Trends Anal. Chem.* **2020**, *123*, 115777.
11. J. Guo, C. Mingoes, X. Qiu, N. Hildebrandt, *Anal. Chem.* **2019**, *91*, 3101.
12. F. Wang, Y. Han, C. S. Lim, Y. Lu, J. Wang, J. Xu, H. Chen, C. Zhang, M. Hong, X. Liu, *Nature* **2010**, *463*, 1061.
13. J. F.-C. Loo, Y.-H. Chien, F. Yin, S.-K. Kong, H.-P. Ho, K.-T. Yong, *Coord. Chem. Rev.* **2019**, *400*, 213042.
14. Q. Liu, B. Wu, M. Li, Y. Huang, L. Li, *Adv. Sci.* **2022**, *9*, 2103911.
15. A. A. Ansari, A. K. Parchur, N. D. Thorat, G. Chen, *Coord. Chem. Rev.* **2021**, *440*, 213971.
16. S. Borse, R. Rafique, Z. V. P. Murthy, T. J. Park, S. K. Kailasa, *Analyst* **2022**, *147*, 3155.
17. C. Severi, N. Melnychuk, A. S. Klymchenko, *Biosens. Bioelectron.* **2020**, *168*, 112515.
18. Z. Li, S. Lu, X. Li, Z. Chen, X. Chen, *Adv. Opt. Mater. 11*, 2202386.
19. S. Bhuckory, S. Lahtinen, N. Höysniemi, J. Guo, X. Qiu, T. Soukka, N. Hildebrandt, *Nano Lett.* **2023**, *23*(6), 2253.
20. K. Nejati, M. Dadashpour, T. Gharibi, H. Mellatyar, A. Akbarzadeh, *J. Cluster Sci.* **2022**, *33*, 1.
21. P. C. Ray, G. K. Darbha, A. Ray, J. Walker, W. Hardy, *Plasmon* **2007**, *2*, 173.
22. Y. Ma, M. Song, L. Li, X. Lao, M.-C. Wong, J. Hao, *Exploration* **2022**, *2*, 20210216.
23. F. Pini, L. Francés-Soriano, V. Andrigo, M. M. Natile, N. Hildebrandt, *ACS Nano* **2023**, *17*, 4971.
24. M. R. Jones, K. D. Osberg, R. J. Macfarlane, M. R. Langille, C. A. Mirkin, *Chem. Rev.* **2011**, *111*, 3736.
25. M. Li, S. K. Cushing, N. Wu, *Analyst* **2015**, *140*, 386.
26. S. Hou, Y. Chen, D. Lu, Q. Xiong, Y. Lim, H. Duan, *Adv. Mater.* **2020**, *32*, 1906475.
27. T. Zhao, T. Li, Y. Liu, *Nanoscale* **2017**, *9*, 9841.
28. A. Wu, Y. Peng, B. Huang, X. Ding, X. Wang, P. Niu, J. Meng, Z. Zhu, Z. Zhang, J. Wang, J. Sheng, L. Quan, Z. Xia, W. Tan, G. Cheng, T. Jiang, *Cell Host Microbe* **2020**, *27*, 325.
29. P. Moitra, M. Alafeef, K. Dighe, M. B. Frieman, D. Pan, *ACS Nano* **2020**, *14*, 7617.
30. X. Zhang, M. R. Servos, J. Liu, *J. Am. Chem. Soc.* **2012**, *134*, 7266.
31. L. Mattsson, K. D. Wegner, N. Hildebrandt, T. Soukka, *RSC Adv.* **2015**, *5*, 13270.
32. B. Wu, Z. Cao, Q. Zhang, G. Wang, *Sens. Actuators B* **2018**, *255*, 2853.
33. Z. Liu, C. Shang, H. Ma, M. You, *Nanotechnology* **2020**, *31*, 235501.
34. L. Francés-Soriano, N. Estebanez, J. Pérez-Prieto, N. Hildebrandt, *Adv. Funct. Mater.* **2022**, *32*, 2201541.
35. M. Wu, X. Wang, K. Wang, Z. Guo, *Chem. Commun.* **2016**, *52*, 8377.
36. M.-K. Tsang, W. Ye, G. Wang, J. Li, M. Yang, J. Hao, *ACS Nano* **2016**, *10*, 598.
37. M. Song, M.-C. Wong, L. Li, F. Guo, Y. Liu, Y. Ma, X. Lao, P. Wang, H. Chen, M. Yang, J. Hao, *Biosens. Bioelectron.* **2023**, *222*, 114987.
38. J. Dong, W. Gao, Q. Han, Y. Wang, J. Qi, X. Yan, M. Sun, *Rev. Phys.* **2019**, *4*, 100026.
39. W. Park, D. Lu, S. Ahn, *Chem. Soc. Rev.* **2015**, *44*, 2940.
40. D. Lu, S. K. Cho, S. Ahn, L. Brun, C. J. Summers, W. Park, *ACS Nano* **2014**, *8*, 7780.
41. C. Clarke, D. Liu, F. Wang, Y. Liu, C. Chen, C. Ton-That, X. Xu, D. Jin, *Nanoscale* **2018**, *10*, 6270.
42. Z. Qi, Q. Wang, Y. Zhai, J. Xu, Z. Tao, Y. Tu, W. Lei, J. Xia, *J. Phys. D Appl. Phys.* **2016**, *49*, 235103.
43. M. Lessard-Viger, D. Brouard, D. Boudreau, *J. Phys. Chem. C* **2011**, *115*, 2974.
44. A. M. Kotulska, A. Pilch-Wróbel, S. Lahtinen, T. Soukka, A. Bednarkiewicz, *Light: Sci. Appl.* **2022**, *11*, 256.
45. M. Lunz, V. A. Gerard, Y. K. Gun'ko, V. Lesnyak, N. Gaponik, A. S. Susha, A. L. Rogach, A. L. Bradley, *Nano Lett.* **2011**, *11*, 3341.
46. H. Zong, X. Wang, X. Mu, J. Wang, M. Sun, *Chem. Rec.* **2019**, *19*, 818.
47. Y. Li, S. Natakorn, Y. Chen, M. Safar, M. Cunningham, J. Tian, D. D.-U. Li, *Front. Phys.* **2020**, *8*, 576862.
48. F. Wang, R. Deng, X. Liu, *Nat. Protoc.* **2014**, *9*, 1634.
49. J. Piella, N. G. Bastús, V. Puntes, *Chem. Mater.* **2016**, *28*, 1066.

SUPPORTING INFORMATION

Additional supporting information can be found online in the Supporting Information section at the end of this article.

How to cite this article: X. Lao, Y. Liu, L. Li, M. Song, Y. Ma, M. Yang, G. Chen, J. Hao, *Aggregate* **2024**, *5,* e448. https://doi.org/10.1002/agt2.448

26924560, 2024, 2, Downloaded from https://onlinelibrary.wiley.com/doi/10.1002/agt2.448 by HONG KONG POLYTECHNIC UNIVERSITY HU NG HOM, Wiley Online Library on [23/09/2024]. See the Terms and Conditions (https://onlinelibrary.wiley.com/terms-and-conditions) on Wiley Online Library for rules of use; OA articles are governed by the applicable Creative Commons License